Title	Electrochemical stability of self-assembled monolayers on nanoporous Au.
Author(s)	Hakamada, Masataka; Takahashi, Masaki; Furukawa, Toshiyuki; Tajima, Kazuki; Yoshimura, Kazuki; Chino, Yasumasa; Mabuchi, Mamoru
Citation	Physical chemistry chemical physics : PCCP (2011), 13(26): 12277-12284
Issue Date	2011-07-14
URL	http://hdl.handle.net/2433/156781
Right	© the Owner Societies 2011.
Type	Journal Article
Textversion	author

Electrochemical stability of self-assembled monolayers on nanoporous Au

Masataka Hakamada,*[a] Masaki Takahashi,[a] Toshiyuki Furukawa,[a] Kazuki Tajima,[b] Kazuki Yoshimura,[b] Yasumasa Chino[b] and Mamoru Mabuchi[a]

Received (in XXX, XXX) Xth XXXXXXXXX 200X, Accepted Xth XXXXXXXXX 200X
First published on the web Xth XXXXXXXXX 200X
DOI: 10.1039/b000000x

Desorption of thiolate self-assembled monolayers (SAMs) seriously limits the fabrication of thiol-based devices. Here we demonstrate that nanoporous Au produced by dealloying Au-Ag alloys exhibits high electrochemical stability against thiolate desorption. Nanoporous Au has many defective sites, lattice strain and residual Ag on the ligament surface. First-principles calculations indicate that these surface aspects increase the binding energy between a SAM and the surface of nanoporous Au.

Introduction

Recently, many researchers have investigated the preparation, characterization, properties and application of nanosized metals and alloys because of their unique electronic, optical, magnetic and catalytic properties, which are considerably different from bulk materials.[1–7] For example, Au and Pd nanoparticles show peculiar magnetic properties different from those of their bulk Au and Pd counterparts.[8,9] It is also known that Au nanoparticles supported on TiO_2 show catalytic properties unlike bulk Au.[10] These findings indicate that the nanosize effect is important for functional development of materials.

As a new class of nanosized metals, nanoporous metals have recently been investigated[11] for their various properties. Nanoporous metals, moreover, can be easily produced through dealloying, that is, selective dissolution of a more active component from a homogeneous alloy.[12] Fabrication techniques and various properties of nanoporous metals have been revealed so far.[13–20]

Several studies utilize self-assembled monolayers (SAMs) that decorate the surface of nanoporous Au.[14,15,20] SAMs are potentially useful in a variety of applications including corrosion inhibition and electron-transfer phenomena, chemical sensors and biomaterials.[21–23] These days, the applications of 4-aminothiophenol (4-ATP) SAMs for sensors and biofuel cells are extensively investigated because of their direct-electron transfer property.[24–29] Their stability against electrochemical disturbance as well as high temperature and pH, however, needs to be improved for practical applications. Several studies have been performed to understand the physical chemistry involved in desorption reaction, in particular, the role of oxygen, ozone, ultraviolet radiation,[30–33] hydrocarbon chain length and end-groups,[34–36] substrate structure,[37–39] and the environment (air, water and organic solutions).[40–44] For the enhancement of the stability of a SAM, the surface structures of substrates are of considerable importance. For example, Cortés et al.[45] investigated the enhanced stability of SAMs on a nanostructured gold substrate. In many cases, the binding energy have been estimated by electrochemical measurements[34,35,45] and X-ray photoelectron spectroscopy (XPS),[46–48] and some theoretical insights into SAMs using first-principles calculations have been reported.[49–52]

In this work, the stability of SAMs adsorbed on nanoporous Au is examined. Nanoporous Au substrates with different pore sizes were prepared by dealloying and subsequent annealing. The electrochemical stability against thiolate desorption was experimentally investigated by cyclic voltammetry (CV) and XPS. The enhanced stability of the nanoporous gold is related to the higher binding energy of thiolate species to the nanoporous Au surface where many defective sites, lattice strains[53] and residual Ag exist. The reasons for the high stability are estimated by first-principles calculations.

Experimental and Computational Methods

Nanoporous Au preparation

Commercially available Au (>99.9 mass%) and Ag (>99.9 mass%) ingots were melted together by arc melting under Ar atmosphere to prepare a precursor $Au_{0.35}Ag_{0.65}$ alloy ingot. After homogenization at 1173 K for 24 h under Ar atmosphere and cold rolling, nanoporous Au was synthesized by dealloying of the alloy (free corrosion) at 253 K for 15 h in 70 mass% HNO_3 (called the 'as-dealloyed' sample in this paper). Some of the sample was freely corroded at room temperature and annealed at 423 K for 15 min under Ar atmosphere to coarsen the porous structure (called the 'coarsened' sample in this paper).

Preparation of 4-ATP SAMs

The thiolate (4-ATP) monolayers were self-assembled on both as-dealloyed and coarsened samples. For the preparation of SAMs on nanoporous Au, the samples were soaked in a 20 mM ethanolic solution of 4-ATP for 65 h at room temperature under laboratory air ambient. After the immersion, the samples were rinsed thoroughly with ethanol and distilled water and dried in air prior to electrochemical measurements and XPS.

Electrochemical measurements

Cyclic voltammetry (CV) was carried out at room temperature to determine the stability of the adsorbed SAMs on nanoporous Au. A three-electrode electrochemical cell with a platinum wire as a counter electrode, the nanoporous Au sample decorated with SAMs as a working electrode and the saturated calomel electrode (SCE) as a reference electrode were used. For comparison, smooth Au surface (polished Au plate) decorated with 4-ATP SAM is also used as a working electrode. CV was conducted under the control by a potentiostat (HZ-5000 by Hokuto Denko). The electrolyte was 0.1 M NaOH degassed for 1 h by N_2 bubbling and the scan rate was 5 mV/s from 0 to −1.2 V. Curves for the first scan are used for consideration.

XPS measurements

XPS (Thermo Electron, Sigma Probe) using Al Kα radiation ($h\nu$ = 1486.6 eV) was employed for the surface elemental analyses of samples. Binding energy scales were referenced by setting the binding energy of Au-$4f_{7/2}$ to 84.0 eV.

Computational details

Geometry optimization calculations were performed using the Cambridge Serial Total Energy Package (CASTEP),[54] in which the density functional theory (DFT)[55,56] was used with a plane wave basis set to calculate the electronic properties of solids from first principles. The exchange–correlation interactions were treated using the spin-polarized version of the generalized gradient approximation (GGA) within the scheme attributable to Perdew-Burke-Ernzerhof (PBE).[57] The ultrasoft pseudopotentials[58] represented in reciprocal space were used for all elements in the calculations. The Kohn-Sham wave functions of valence electrons were expanded to the plane wave basis set within a specified cutoff energy (= 340 eV). The Brillouin zone was sampled using a Monkhorst-Pack 3 × 3 × 1 k-point mesh in the defective-surface models and 5 × 5 × 1 k-point mesh in the residual Ag models and the Gaussian smearing with 0.1 eV width.

In the defective surface models, calculations were performed using face-centered-cubic (111) surface slab models for the 3 × 3 supercells of the (1 × 1) unit cell in nine different surface models for comparison of reported works.[51,52] In the residual Ag models, on the other hand, calculations were performed using the surface slab models for the 2 × 2 supercells of the (1 × 1) unit cell in four different models.[59] A five-atomic-layer model was employed for all the models, and two bottom layers were constrained while the rest were allowed to relax. The repeated slabs were separated from each other by a vacuum space of 10 Å. In this calculation, methanethiol (MT), instead of 4-ATP, was employed as the thiolate species for calculation efficiency.

Results

Scanning electron microscopy (SEM) confirmed the formation of as-dealloyed and coarsened nanoporous Au, as shown in Fig. 1. Analyses of SEM images (more than 100 pores for each sample) revealed that the average pore sizes, where each

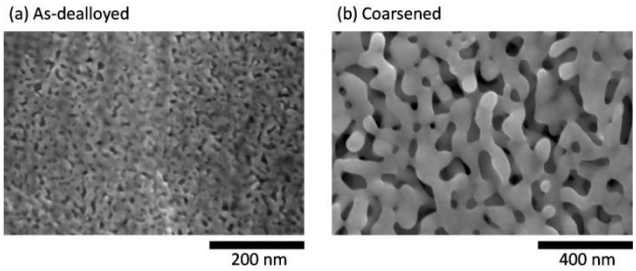

Fig. 1 Scanning electron microscopy images of (a) as-dealloyed and (b) coarsened nanoporous Au samples.

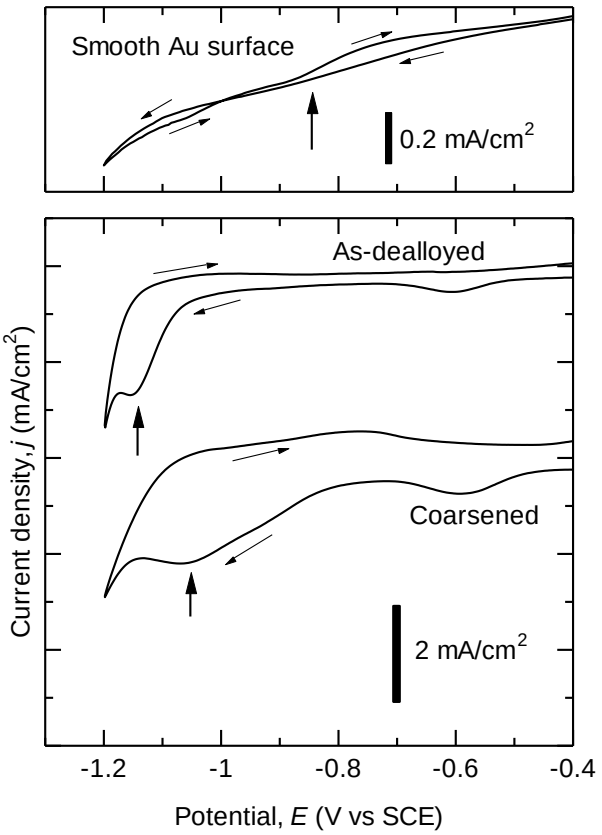

Fig. 2 Cyclic voltammetric curves of as-dealloyed and coarsened nanoporous Au samples decorated with 4-ATP SAMs. The electrolyte used was 0.1 M NaOH and the scan rate was 5 mV/s.

pore size was determined as the distance between adjacent ligaments, were approximately 6 and 40 nm for as-dealloyed and coarsened samples, respectively. As-dealloyed nanoporous Au exhibited a highly irregular pore shape.

Typical CV curves for as-dealloyed and coarsened nanoporous Au after SAM decoration are shown in Fig. 2. CV curves for smooth Au surface is also included there. The CV curves for nanoporous Au exhibited a clear reductive peak during cathodic scan, which shows that both nanoporous samples are successfully decorated with SAMs. The cathodic potential scan of both curves shows major current peaks below −1.0 V. The major peak (indicated by arrows) corresponds to the reductive desorption of 4-ATP SAMs from Au surfaces.[29,60] The peak potential (= −1.15 V) of as-dealloyed nanoporous Au decorated with 4-ATP SAMs was

lower than that (= −1.05 V) of the coarsened one. Less significant broadened peaks within the potential range from −0.50 to −0.70 V, which seem to be associated with a phase transition occurring at the phenyl ring,[29,60] were also found in both cathodic curves. Moreover, the broadened anodic peak at −0.75 V during the reverse scan was found only in the curve for the coarsened sample. On the other hand, only broad peak around −0.84 V is observed in the cathodic CV curve for smooth Au surface. Anodic peak at −0.75 V is also found.

The real surface area measurement (CV in 0.5 M H_2SO_4) showed that the thiol surface coverage was approximately 0.02, which is apparently low; for example, SAM of nonanethiol shows surface coverage of 0.15–0.30.[45] The low coverage may be attributed to phenyl ring in 4-ATP which occupies larger space than simple carbon chain in alkanethiol.

The results of XPS analyses of the samples before and after CV measurements are shown in Fig. 3. Sulfur (S-2p, binding energy of 160.8–164.2 eV) and nitrogen (N-1s, binding energy of 398.3–403.0 eV, not shown in Fig. 3 for simplicity) were detected from both samples. This fact implies that as-dealloyed and coarsened nanoporous Au were successfully decorated with SAMs. The peak intensity for the as-dealloyed sample is higher than that for the coarsened sample, which suggests that the as-dealloyed nanoporous Au causes a significant adsorption of SAMs. Moreover, the XPS analyses of the samples after CV measurements revealed that the S-2p peak was weakened to a noticeable degree for the as-dealloyed nanoporous Au, but that little degradation of the S-2p peak intensity was observed for the coarsened sample. Nevertheless, the S-2p peak intensity from the as-dealloyed sample after CV was still higher than that from the coarsened sample before and after CV.

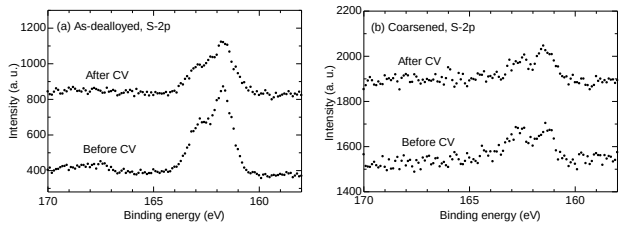

Fig. 3 S-2p X-ray photoelectron spectra from (a) as-dealloyed and (b) coarsened nanoporous Au decorated with SAMs of 4-ATP before and after CV.

Discussion

CV curves and SAM stability

In the CV curves, the as-dealloyed nanoporous Au exhibited the peak of SAM desorption at a more negative potential than the coarsened sample. These peak potentials are, however, far more negative than those for smooth Au surface. It has been reported that the more negative the potential of the desorption peak, the stronger the bonding between SAMs and the Au surface;[45,61] hence, the bonding between 4-ATP SAMs and surface of as-dealloyed nanoporous Au is stronger than that between SAMs and the surface of the coarsened sample. Thus, the as-dealloyed nanoporous Au provides a higher electrochemical stability of SAMs of 4-ATP than the coarsened one. However, compared with 4-ATP on the gold thin film, the desorption potential of which was reported to be −0.735 V under the same condition,[29] both nanoporous Au samples offer a much higher binding energy between the Au surface and SAMs.

Moreover, a broadened peak at −0.75 V during reverse scan was found for the coarsened sample, while no peak was observed for the as-dealloyed sample. The broadened anodic peak at approximately −0.75 V is related to a partial readsorption of monolayers on the Au surface.[29,62] The present results indicate that almost no rebinding of 4-ATP occurred in the as-dealloyed sample and that some 4-ATP molecules adsorbed again in the coarsened sample during the anodic scan.

Such presence and absence of molecular readsorption during the anodic scan are also suggested from the XPS results shown in Fig. 3; that is, degradation in the intensity of the S-2p peak can be found after CV of the as-dealloyed sample, perhaps because of the absence of the readsorption of 4-ATP. The intensity of S-2p spectra of the coarsened sample, however, was almost unchanged by CV, indicating that the 4-ATP, which had been released during the cathodic scan, was adsorbed again during the anodic scan. No readsorption of 4-ATP occurred in the as-dealloyed sample, perhaps because the 4-ATP, just after the cathodic scan, remains at a much higher density on the surface of the as-dealloyed nanoporous Au than on the surface of the coarsened sample owing to the enhanced binding energy. This situation is supported by the higher S-2p peak even after CV of the as-dealloyed sample than the peak before CV of the coarsened sample, suggesting that more SAMs are adsorbed at the as-dealloyed nanoporous Au. A large amount of absorbed molecules remains at a very high density on the as-dealloyed samples after the cathodic scan such that there is very little space on which desorbed molecules can be readsorbed. On the other hand, there are much less adsorbed monolayers on the coarsened nanoporous Au than on the as-dealloyed one; many of the desorbed 4-ATP molecules can be readsorbed on the surface of the coarsened nanoporous Au during the reverse anodic scan.

The enhanced bonding between Au and S on the surface of the as-dealloyed nanoporous Au is also suggested by the fact that the oxidized states of sulfur in the two samples significantly differ, as shown in Fig. 3. The XPS peak component at 163.5 eV, which implies the existence of unbound sulfur species,[47] is as high as that at 162.1 eV corresponding to bound thiol[47] for the coarsened nanoporous Au decorated with SAMs. However, the peak for bound sulfur species is more significant in the spectrum of as-dealloyed nanoporous Au decorated with SAMs. The fractions of bound thiol in the as-dealloyed and coarsened sample are estimated to be 0.66 and 0.33, respectively, by curve fitting. Thus, the as-dealloyed nanoporous Au with a small pore size of 6 nm offers enhanced electrochemical stability of adsorbed SAMs.

DFT approach for SAM stability in nanoporous Au

Surface straining and defects

To confirm the mechanism underlying the higher binding

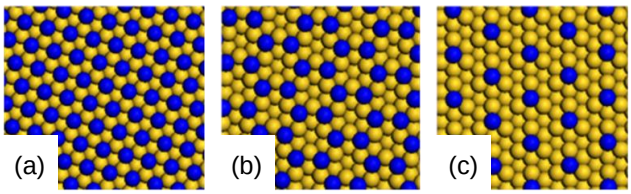

Fig. 4 Optimized structures for Au (111) surface for (a) perfect, (b) honeycomb and (c) adatom models. Yellow spheres are internal Au atoms and blue spheres are Au surface atoms in the first surface layer.

energy of Au-S in the as-dealloyed sample, first-principles calculations were performed. There are many lattice strains and defective sites on nanoporous metals such as adatoms, vacancies and steps because of the complex and nanosized three-dimensional curvature of surfaces.[53] Such defective sites are responsible for SAM stability,[45] and hence, the adsorption energy of MT on a perfect Au (111) surface (Fig. 4a) and Au (111) surfaces containing vacancy-like honeycomb (Fig. 4b) and adatom (Fig. 4c) structures. MT molecules were located at a bridge site between two adjacent surface atoms in perfect and honeycomb models and at the a-top site (just above the adatom) in the adatom model. Moreover, in each model, cell sizes were varied by ±5% to determine the effect of lattice contraction and expansion.

Figure 5 shows the calculated absorption energy of MT onto each model of the Au (111) surface. At the strain of 0%, both adatom and honeycomb surface structures reduced the adsorption energy, compared with the perfect (111) surface; thus, it is suggested that these defective surface structures cause higher stabilities the than perfect Au (111) surface. On the other hand, lattice strain, irrespective of contraction and expansion, seems to affect adsorption energy of MT less significantly than the surface defects. Figure 6 shows the local density of states (LDOS) of Au atoms bonded with MT in perfect, honeycomb and adatom models (with no straining). As reported in the case of hydrogen adsorption,[53,63] an increase in the energy gap ($\Delta\varepsilon$) between the bottom of Au and the split-off S-Au bonding state would strengthen the S-Au bond. Therefore, the larger split-off states in the honeycomb model lead to the lowered adsorption energy (and then stable adsorption) of MT. On the other hand, no difference was found in the energy gap $\Delta\varepsilon$ between the perfect and adatom models; however, the peak of the S-Au bonding state in the adatom model was higher than that of the perfect model. Furthermore, a new peak at around −17 eV, which was not seen in the perfect model, was found in the adatom model. Defective sites at the surface, therefore, strengthen the bonding between Au and S atoms.

Figure 5 shows that lattice expansion (+5% strain) also reduces the adsorption energy of MT in the perfect and honeycomb models, but that, the lattice expansion in the adatom model has a negative effect on the adsorption of MT. Thus, lattice strains may not always strengthen S-Au bonding. Figure 7 shows LDOS of perfect Au (111) models with ±5% strains. Comparison of LDOS shows that the energy gap between the bottom of the Au band and the split-off S-Au bonding state increased with the increase in strain (and thus, the decrease in the adsorption energy of MT), as reported in

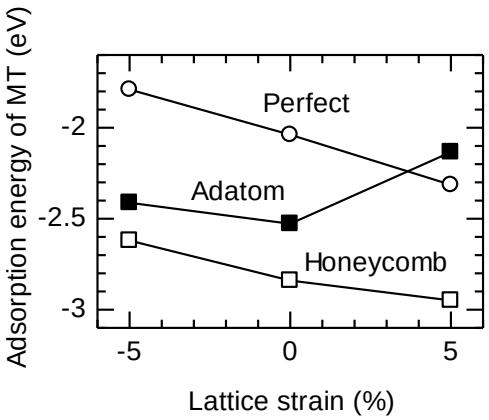

Fig. 5 Effects of surface defective structures and lattice strains on adsorption energy of methanethiol on Au (111) surfaces estimated by first-principles calculations.

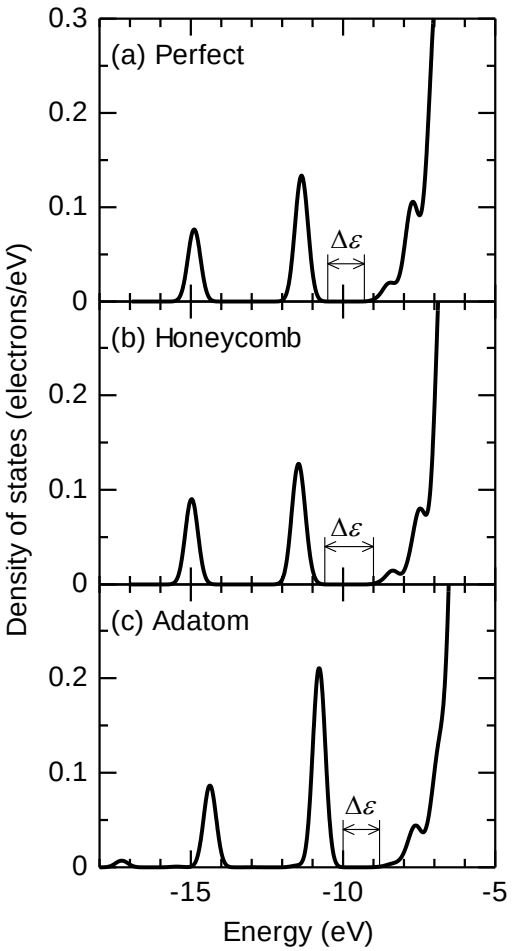

Fig. 6 Local density of states (LDOS) of Au atoms bound with methanethiol in (a) perfect, (b) honeycomb and (c) adatom models with no strain. Larger split-off between Au band and S-Au bonding is present in honeycomb model and one new peak can be observed around −17 eV in adatom model.

the case of hydrogen adsorption on the Pd surface.[53] Figure 8 shows LDOS of ±5%-strained honeycomb Au (111) models, indicating a similar trend in the energy gap between the split-

off state and bottom edge of the Au band. However, LDOS of +5%-strained adatom Au models, as shown in Fig. 9, had a smaller energy gap between the split-off state and edge of the Au band than that of the adatom Au model with no strain. This is in agreement with the fact that the +5%-strained adatom model showed a higher adsorption energy of MT (or less stability of MT adsorption) than the no-strain adatom model (Fig. 5). Thus, the effect of strain on the adsorption energy can be viewed in terms of the energy gap between the split-off state and the Au band bottom.

The electron density distribution also reflects the trend in the adsorption energy of MT, as shown in Fig. 10, which summarizes the charge density maps at the Au (111) surface of perfect, honeycomb and adatom models with and without straining. In the honeycomb and perfect models, the more expanded the lattice, the lower the electron density between atoms. This result indicates that, as the lattice is expanded, the electron density near the Au atoms becomes much higher, so that more electrons contribute to the S-Au bond. The adatom models, on the other hand, exhibit a different trend in the electron density distribution. That is, the adatom models with −5% and 0% strains have isotropic electron distribution, but electrons in the +5%-strained adatom model spread anisotropically. Such an irregular shape of electron distribution would cause electron starvation around Au adatoms and subsequent weakening of the S-Au bond.

Residual Ag

Nanoporous Au is fabricated through selective dealloying of Ag from Au-Ag alloys; however, some portion of Ag inevitably remains in the material. The residual Ag, in several cases,[64] segregates at the surface of nanoporous Au even after the complete macroscopic removal of Ag. XPS on the as-dealloyed and coarsened nanoporous Au (Fig. 11) revealed

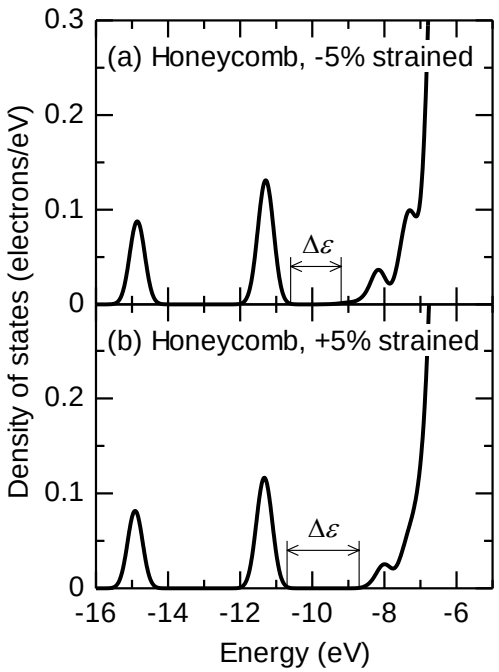

Fig. 8 Local density of states (LDOS) of Au atoms bound with methanethiol in honeycomb model with (a) −5% (contracted) and (b) +5% (expanded) strains. The split-off between the Au band and S-Au bonding is larger in the +5% strained model than in the −5% strained model.

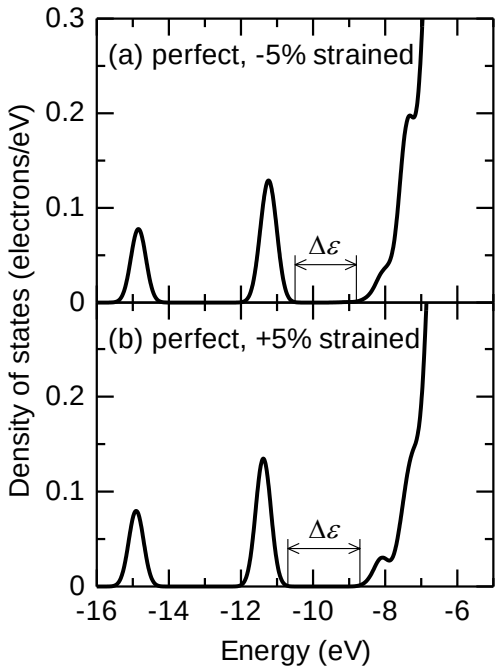

Fig. 7 Local density of states (LDOS) of Au atoms bound with methanethiol in perfect model with (a) −5% (contracted) and (b) +5% (expanded) strains. The split-off between the Au band and S-Au bonding is larger in the +5% strained model than in the −5% strained model.

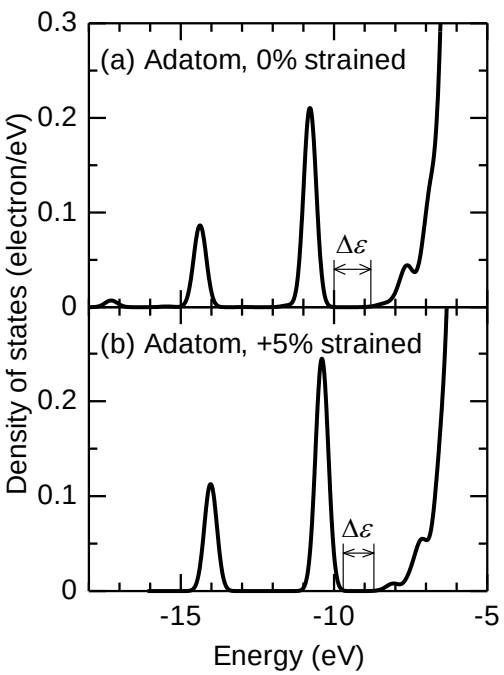

Fig. 9 Local density of states (LDOS) of Au atoms bound with methanethiol in adatom model with (a) 0% and (b) +5% (expanded) strains. The split-off between the Au band and S-Au bonding is smaller in the +5% strained model than in the 0% strained model.

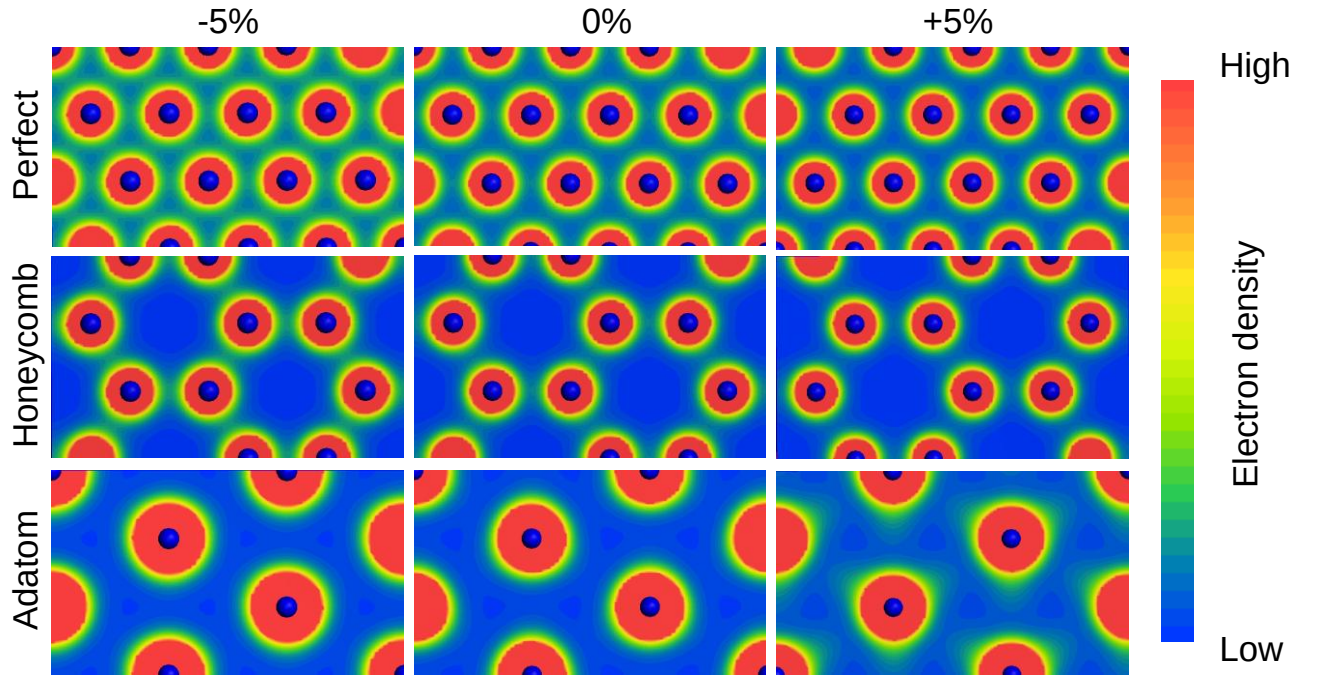

Fig. 10 Surface charge density maps of Au (111) models. In the +5% strained perfect and honeycomb models, the density of electrons between atoms was lower than that in the −5% strained models. Such a degradation of electron density causes the concentration of electrons around Au atoms. In the adatom model, no significant difference can be observed between −5% and 0% strained models; but the +5% strained model has an irregular electron distribution around Au atoms. Therefore, electrons spread out between atoms, and fewer electrons contribute to the S-Au bonding.

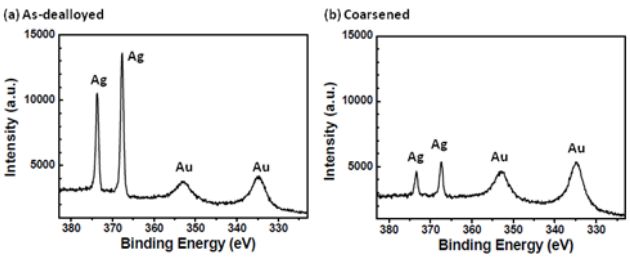

Fig. 11 X-ray photoelectron spectra from (a) as-dealloyed and (b) coarsened nanoporous Au showing surface concentration of Ag and Au.

that the approximate surface Ag concentrations were 50 at.% for the as-dealloyed sample and 15 at.% for the coarsened sample. That is, more Ag atoms are segregated on the ligament surface of the as-dealloyed sample. Kawasaki and Iino[61] reported that the packing density of SAMs increased when the substrate Au is alloyed with Ag. Thus, the surface-segregated Ag in the present nanoporous Au may affect the stability of a SAM.

DFT calculations, therefore, were also conducted to estimate the residual Ag effects. One Au atom was replaced by one Ag atom in the three models where the positions of the Ag atom were different. The surface Ag model contains one Ag atom at the (111) surface, whereas the second- and third-layer Ag models contain one Ag atom in the second and third layers, respectively, as illustrated in Figs. 12a–c. The model without the Ag replacement (Ag-free model) was also subjected to DFT calculations. MT molecules were located at bridge sites between two adjacent Au atoms in each model. Table 1 summarizes the calculation results for the adsorption

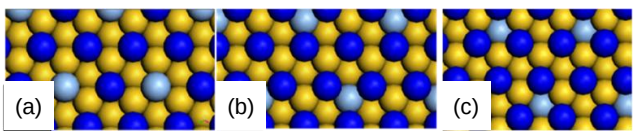

Fig. 12 Optimized structures for Au (111) surface with residual Ag. (a) Surface Ag, (b) second-layer Ag and (c) third-layer Ag models. Yellow spheres are internal Au atoms, blue spheres are Au surface atoms in the first surface layer and gray spheres are Ag atoms.

Table 1 Adsorption energies and bonding electron numbers below Fermi level around Au atom in residual Ag models. MT molecules are located at bridge sites between two adjacent Au atoms at (111) surface

Models	Surface Ag	2nd-layer Ag	3rd-layer Ag	Ag-free
Binding energy (eV)	−2.04	−1.87	−1.89	−1.91
Electron number	11.20	11.14	11.13	11.12

energies of MT on the Ag-containing models. The surface Ag model showed the lowest adsorption energy of MT, which suggests that Ag residually segregated at the surface enhances S-Au bonding. The second- and third-layer models, however, have almost the same MT adsorption energy as the Ag-free model. These results suggest that the Ag atoms inside the materials have a less significant effect on S-Au bonding than the Ag atoms segregated at the surface.

LDOS of residual Ag and Ag-free models are presented in Fig. 13. In the surface Ag model, the energy gap $\Delta\varepsilon$ between the split-off S-Au bonding state and Au band bottom was larger than that in the Ag-free model, like defective surface models, while the $\Delta\varepsilon$ in the second- and third-layer models is

similar to that in the Ag-free model. Calculations of bonding electron numbers by integrating total DOS below the Fermi level also indicate that the bonding electron number (= 11.20) around the Au atom bound with MT in the surface Ag model is larger than that (= 11.12) in the Ag-free model, while no essential difference is found in the electron numbers around Au atoms bound with MT in the Ag-free, second-layer Ag and third-layer Ag models. Such an increase in electron density in surface Ag model strengthens the S-Au bonding. That is, residual Ag segregated at the surface of the ligament has a much more significant effect on the S-Au bonding than the Ag left inside the ligament. Thus, the residual surface Ag is important in the present case, as reported in the case of CO oxidation.[64]

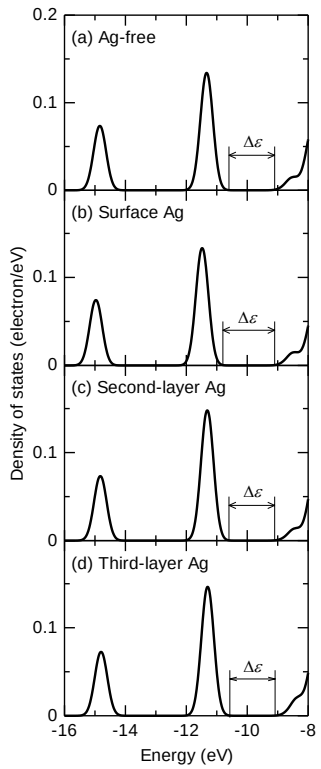

Fig. 13 Local density of states (LDOS) of Au atoms bound with methanethiol in (a) Ag-free, (b) surface Ag, (c) second-layer Ag and (d) third-layer Ag models. The split-off between the Au band and S-Au bonding is larger in the +5% strained model than in the −5% strained model.

Conclusions

The stability of a SAM on nanoporous Au was examined by CV and it is suggested that smaller nanopores offer higher SAM stability. Nanoporous Au can be fabricated by dealloying homogeneous Ag-Au alloys in an electrolyte where a large surface is coercively created; there are many defect sites and residual Ag atoms at the surface of the nanoporous Au. First-principles calculations suggested that the defects and residual Ag at the surface of nanoporous Au markedly contribute to the SAM stabilization. Therefore, nanoporous Au is an attractive material as a substrate for excellent thiolate-based devices. We emphasize that nanoporous Au can be easily prepared through dealloying, and its high surface area and minute pore size can be controlled in a systematic way. These points will be effective for devices such as biosensors[27,29] and enzyme biofuel cells.[65] Further studies are required to control surface defects and residual Ag of nanoporous Au for practical application.

Acknowledgements

This study was partially supported by JSPS Grant-in-Aid for Challenging Exploratory Research (KAKENHI, 22656155).

Notes and references

[a] *Department of Energy Science and Technology, Graduate School of Energy Science, Kyoto University, Kyoto 606-8501, Japan. Fax: +81 75 753 5428; Tel:+81 75 753 5427; E-mail: hakamada.masataka.3x@kyoto-u.ac.jp*

[b] *Materials Research Institute for Sustainable Development, National Institute of Advanced Industrial Science and Technology (AIST), Moriyama, Nagoya 463-8560, Japan.*

† Electronic Supplementary Information (ESI) available: CV curve for nanoporous Au without SAM. See DOI: 10.1039/b000000x/

1 P. V. Kamat, *Chem. Rev.*, 1993, **93**, 267.
2 B. C. Gates, *Chem. Rev.*, 1995, **95**, 511.
3 L. L. Beecroft and C. K. Ober, *Chem. Mater.*, 1997, **9**, 1302.
4 L. Brus, *J. Phys. Chem.*, 1986, **90**, 2555.
5 D.-H. Chen, S.-H. Wu, *Chem. Mater.*, 2000, **12**, 1354.
6 F. C. Fonseca, F. C. Goya, R. F. Jardim, *Phys. Rev. B*, 2002, **66**, 104406.
7 C. Liu and Z. J. Zhang, *Chem. Mater.*, 2001, **13**, 2092.
8 Y. Yamamoto, M. Miura, M. Suzuki, N. Kawamura, N. Miyagawa, T. Nakamura, K. Kobayashi, T. Teranishi and H. Hori, *Phys. Rev. Lett.*, 2004, **93**, 116801.
9 B. Sampedro, P. Crespo, A. Hernando, R. Litrán, J. C. S. López, C. L. Cartes, A. Fernandez, J. Ramírez and J. G. Calbet and M. Vallet, *Phys. Rev. Lett.*, 2003, **91**, 237203.
10 M. Haruta, S. Tsubota, T. Kobayashi, H. Kageyama, M. J. Genet and B. Delmon, *J. Catal.*, 1993, **144**, 175.
11 Y. Ding and M. Chen, *MRS Bulletin*, 2009, **34**, 569.
12 J. Erlebacher, M. J. Aziz, A. Karma, N. Dimitrov and K. Sieradzki, *Nature*, 2001, **410**, 450.
13 M. Hakamada and M. Mabuchi, *Nano. Lett.*, 2006, *6*, 882–885.
14 D. Robinson, C.-A. M. Wu, M. D. Ong, B. W. Jacobs and B. E. Pierson, *Langmuir*, 2010, **26**, 6797.
15 P. N. Ciesielski, A. M. Scott, C. J. Faulkner, B. J. Berron, D. E. Cliffel and G. K. Jennings, *ACS Nano*, 2008, **2**, 2465.
16 S. O. Kucheyev, J. R. Hayes, J. Biener, T. Huseer, C. E. Talley and A. V. Hamza, *Appl. Phys. Lett.*, 2006, **89**, 053102.
17 X. Ge, R. Wang, P. Liu and Y. Ding, *Chem. Mater.*, 2007, **19**, 5827.
18 X. Wang, W. Wang, Z. Qi, C. Zhao, H. Ji and Z. Zhang, *J. Power Sources*, 2010, **195**, 6740.
19 C. Xu, L. Wang, X. Mu and Y. Ding, *Langmuir*, 2010, **26**, 7437.
20 M. C. Dixon, T. A. Daniel, M. Hieda, D. M. Smilgies, M. H. Chan and D. L. Allara, *Langmuir*, 2007, **23**, 2414.
21 A. Ulman, *Chem. Rev.*, 1996, **96**, 1533.
22 J. C. Love, L. A. Estroff, J. K. Kriebel, R. G. Nuzzo and G. M. Whitesides, *Chem. Rev.*, 2005, **105**, 1103.
23 F. Schreiber, *Prog. Surf. Sci.*, 2000, **65**, 151.
24 G. Gupta, V. Rajendran, P. Atanassov, *Electroanalysis*, 2004, **16**, 1182.
25 M. Pita, S. Shleev, T. Ruzgas, V. M. Fernández, A. I. Yaropolov, L. Gorton, *Electrochem. Comm.*, 2006, **8**, 747.
26 S. Shleev, M. Pita, A. I. Yaropolov, T. Ruzugas, L. Gorton, *Electroanalysis*, 2006, **18**, 1901.
27 G. Gupta, R. Rajendran and P. Atanassov, *Electroanalysis*, 2003, **15**, 1577.
28 F. Li, W. Chen, P. Dong and S. Zhang, *Biosens. Bioelectron.*, 2009, **24**, 2160.

29 E. Valério, M. Abrantes and S. Viena, *Electroanalysis*, 2008, **20**, 2467.
30 T. M. Willey, A. L. Vance, T. Buuren, C. Bostedt, L. J. Terminello and C. S. Fadley, *Surf. Sci.*, 2005, **576**, 188.
31 M. Lewis and M. Tarlov, *J. Am. Chem. Soc.*, 1995, **117**, 9574.
32 D. A. Hutt and J. Leggett, *J. Phys. Chem.*, 1996, **100**, 6557.
33 Y. Zhang, R. H. Terrill and P. W. Bohn, *Chem. Mater.*, 1999, **11**, 2191.
34 C. A. Widrig, C. Chung and M. D. Porter, *J. Electroanal. Chem.*, 1991, **310**, 335.
35 M. E. Vela, H. Martin, C. Vericat, G. Andreasen, H. Creus and R. C. Salavarezza, *J. Phys. Chem. B*, 2000, **104**, 11878.
36 E. Ito, J. Noh and M. Hara, *Chem. Phys. Lett.*, 2008, **462**, 209.
37 C. M. Whelan, C. J. Barnes, C. Grégoire and J.-J. Piereaux, *Surf. Sci.*, 2000, **454**–**456**, 67.
38 J. Stettner, P. Frank, T. Griesser, G. Trimmel, R. Schnnach, E. Gilli and A. Winkler, *Langmuir*, 2009, **25**, 1427.
39 M.-T. Lee, C.-C. Hsueh, M. S. Freund and G. S. Ferguson, *Langmuir*, 1998, **14**, 6419.
40 M. H. Schoenfisch and J. E. Pemberton, *J. Am. Chem. Soc.*, 1998, **120**, 4502.
41 G. Mani, D. M. Johnson, D. Marton, V. L. Dougherty, M. D. Feldman, D. Patel, A. A. Ayon and C. M. Agrawal, *Langmuir*, 2008, **24**, 6774.
42 M. S. E.-Deab and T. Ohsaka, *Electrochim. Acta*, 2004, **49**, 2189.
43 N. Garg, E. C.-Molina and T. R. Lee, *Langmuir*, 2002, **18**, 2717.
44 G. Yang, N. A. Amro, Z. B. Starkwolfe, G.-Y. Liu, *Langmuir*, 2004, **20**, 3995.
45 E. Cortés, A. A. Rubert, G. Benitez, P. Carro, M. E. Vela, R. C. Salvarezza, *Langmuir*, 2009, **25**, 5661.
46 M. Onoue, M. R. Han, E. Ito and M. Hara, *Surf. Sci.*, 2006, **600**, 3999.
47 D. G. Castner, K. Hinds and D. W. Grainger, *Langmuir*, 1996, **12**, 5083.
48 M. Wirde and U. Gelius, *Langmuir*, 1999, **15**, 6370.
49 M. Yu, N. Bovet, C. J. Satterley, S. Bengió, K. R. J. Lovelock, P. K. Milligan, R. G. Jones, D. P. Woodruff and V. Dhanak, *Phys. Rev. Lett.*, 2006, **97**, 166102.
50 R. Mazzarello, A. Cossaro, A. Verdini, R. Rousseau, L. Casalis, M. F. Danisman, L. Floreano, S. Scandolo, A. Morgante and G. Scoles, *Phys. Rev. Lett.*, 2007, **98**, 016102.
51 L. M. Molina and B. Hammer, *Chem. Phys. Lett.*, 2002, **360**, 264.
52 P. Carro, R. Salvarezza, D. Torres and F. Illas, *J. Phys. Chem. C*, 2008, **112**, 19121.
53 M. Hakamada, H. Nakano, T. Furukawa, M. Takahashi and M. Mabuchi, *J. Phys. Chem. C*, 2010, **114**, 868.
54 M. C. Payne, M. P. Teter, D. C. Allan, T. A. Arias and J. D. Joannopoulos, *Rev. Mod. Phys.*, 1992, **64**, 1045.
55 P. Hohenberg, W. Kohn, *Phys. Rev.*, 1964, **136**, B864.
56 W. Kohn, L. J. Sham, *Phys. Rev.*, 1965, **140**, A1133.
57 J. P. Perdew, K. Burke and M. Ernzerhof, *Phys. Rev. Lett.*, 1996, **77**, 3865.
58 D. Vanderbilt, *Phys. Rev. B*, 1990, **41**, 7892.
59 J. Zhang, H. Jin, M. B. Sullivan, F. C. H. Lim, P. Wu, *Phys. Chem. Chem. Phys.*, 2009, **11**, 1441.
60 T. Komura, T. Yamaguchi, H. Shimatani and R. Okushio, *Electrochim. Acta*, 2004, **49**, 597.
61 M. Kawasaki and M. Iino, *J. Phys. Chem. B*, 2006, **110**, 21124.
62 C.-J. Zhong, J. Zak and M. D. Porter, *J. Electroanal. Chem.*, 1997, **421**, 9.
63 D. Tománek, Z. Sun and S. G. Louie, *Phys. Rev. B*, 1991, **43**, 4699.
64 A. Wittstock, B. Neumann, A. Schaefer, K. Dumbuya, C. Kübel, M. M. Biener, V. Zielasek, H.-P. Steinrück, J. M. Gottfried, J. Biener, A. Hamza and M. Bäumer, *J. Phys. Chem. C*, 2009, **113**, 5593.
65 L. Deng, F. Wang, H. Chen, L. Shang, L. Wang, T. Qang and S. Dong, *Biosens. Bioelectron.*, 2008, **24**, 329.